Materials Science & Engineering A 627 (2015) 270–276

Contents lists available at ScienceDirect

Materials Science & Engineering A

journal homepage: www.elsevier.com/locate/msea

The effect of aging on the microstructure and mechanical behavior of the alumina-forming austenitic stainless steel Fe–20Cr–30Ni–2Nb–5Al

Geneva Trotter, Ian Baker*

Thayer School of Engineering, Dartmouth College, Hanover, NH 03755, USA

ARTICLE INFO

Article history:
Received 26 November 2014
Received in revised form
16 December 2014
Accepted 18 December 2014
Available online 14 January 2015

Keywords:
Mechanical characterization
Austenite
Intermetallics
Aging
Grain boundaries
Precipitation

ABSTRACT

The effect of aging on the microstructure and mechanical behavior of an alumina-forming austenitic stainless steel, Fe–20Cr–30Ni–2Nb–5Al (at%) has been investigated. The alloy was fully solutionized after a 1250 °C, 24 h heat treatment, and the precipitation of B2 and Laves phases was studied after aging at 800 °C for up to 1325 h. While after 24 h the Laves phase precipitates in the matrix were 205 nm in diameter, they showed a further increase in diameter of only 50 nm even after aging for 1325 h. In contrast, the B2 precipitates in the matrix grew at a faster rate: after first being observed after aging for 24 h at an average diameter of 194 nm, they more than doubled in size from 330 to 734 nm as the aging time increased from 240 h to 1325 h. Both the Laves and B2 precipitates in the grain boundaries grew at a faster rate and were larger than matrix precipitates. The grain boundary coverage at 2.4 h (Laves 192 nm, NiAl 126 nm) was 56% with Laves phase initially making up the bulk of the precipitates, but after 2.4 h Laves phase and B2 precipitates alternated on the grain boundaries and total coverage reached 93% after 1325 h. An increase in the volume fraction of precipitates in the alloy was accompanied by an increase in the yield strength from 205 MPa after the solutionizing treatment up to 383 MPa after aging at 800 °C for 1325 h. After aging for 1325 h, even with extensive intermetallic grain boundary coverage, the alloy showed a room temperature elongation of 19%.

1. Introduction

The materials needed for energy applications have traditionally been those that maximize efficiency and decrease costs. Alumina-forming austenitic (AFA) stainless steels have shown promise to decrease reliance on expensive Ni-base alloys for aggressive conditions in energy production and chemical processing environments [1]. AFAs use alumina as a protective oxide scale for high corrosion resistance instead of chromia; alumina is known to offer even better protection than chromia at high temperatures [2,3]. AFA stainless steels were in development as early as the 70s [4] and more recently a new family of AFAs has been developed at the Oak Ridge National Laboratory (ORNL) [1,5–8].

The newer grades of AFA stainless steels have an austenitic matrix, which provides better high-temperature creep strength than a b.c.c. matrix, and either MC or γ′-Ni_3Al precipitates provide creep strengthening [1,7,8]. AFA stainless steels, which exist over a wide compositional range, have shown promising results but further study is needed to find the optimum combination of alloying elements that provide the most effective creep strengtheners at reasonable cost for commercialization [1]. Even within particular grades of AFAs, the influence of precipitate phases on creep strength is complex and a wide variety of creep strengths can be obtained with relatively small changes in alloying elements and phases [1,9,10].

Laves phase precipitates are potential candidates for strengthening AFA stainless steels. The AB_2-type Laves phase generally comes in one of three forms: hexagonal $MgZn_2$ (C14), cubic $MgCu_2$ (C15) or hexagonal $MgNi_2$ (C36) [11]. Even though Laves phase has been shown to be harmful in some ferritic steels [12], decreasing their toughness and strength and precipitating at the grain boundaries, some research has indicated their potential for strengthening in both AFA stainless steels and alloys with similar compositions [7,10,13–16]. Use of the C14 Fe_2Nb as a strengthener in an AFA steel is advantageous because it has a high melting temperature of 1641 °C, exists in equilibrium with f.c.c. γ-Fe to temperatures above 955 °C [13,17], and has shown long-term stability at high temperatures [7,16–18]. Some previous studies have looked to Laves phase particles for strengthening in AFA-type alloys, but have only seen low or moderate improvements in creep resistance [7,16]. There was a slight improvement in creep resistance at 750 °C and 100 MPa in an AFA steel when the niobium content increased from 1 to 2 at% but the improvement

* Correspondence to: 14 Engineering Drive, Dartmouth College, Hanover, NH 03755, USA. Tel.: +1 603 646 2184.
E-mail address: Ian.Baker@dartmouth.edu (I. Baker).

http://dx.doi.org/10.1016/j.msea.2014.12.072
0921-5093/

was small when compared to the effect of increased carbon content. There was some dislocation pinning by coarse 500 nm size Fe_2Nb precipitates and 10-nm size MC carbide precipitates but it was not clear whether the combination of precipitates was better than strengthening by MC carbide alone [16].

In the present work, the effects of heat treatment on the microstructure and mechanical behavior of an alumina-forming austenitic stainless steel, Fe–20Cr–30Ni–2Nb–5Al (at%) have been investigated. We show that, despite extensive intermetallic coverage of the grain boundaries, surprisingly, the material was able to show both good ductility and strength.

2. Experimental

15.24 cm long, 2.54 cm diameter ingots of Fe–20Cr–30Ni–2Nb–5Al (at%) were arc melted followed by drop casting into a copper crucible, courtesy of Dr. Easo P. George at ORNL. The as-cast alloy was homogenized in argon for 24 h at 1250 °C and water quenched. This homogenization treatment produces a single phase material [19]. Samples were subsequently aged in air for 2.4 h, 24 h, 240 h, 480 h and 1325 h at 800 °C.

A FEI XL-30 field emission gun (FEG) scanning electron microscope (SEM) operated at 15 kV and equipped with energy dispersive spectroscopy (EDS) was used for microstructural analysis. Samples were prepared for SEM analysis by polishing with successively finer grits of silicon carbide paper, up to 1200 and with 0.3 and 0.05 μm alumina powder in a water to obtain a mirror finish. Backscattered electron (BSE) images from the specimens were processed using ImageJ [20] using a routine described in a previous paper [19] that uses *Z*-contrast to distinguish precipitates.

Transmission electron microscope (TEM) specimens were prepared by cutting discs out of samples that had been milled into 3 mm cylindrical rods. These discs were mechanically thinned and polished to ~100 μm thick and electropolished using a Struers TenuPol-5 twin-jet electropolisher at a voltage of 11 V with a current of ~180 mA using an electrolyte of 25% nitric acid in methanol at −20 °C. An EDS-equipped FEI Tecnai FS20ST FEG TEM operated at 200 kV was used to examine specimens.

Flat, dog-bone tensile specimens approximately 1.27 mm thick, with an overall length of 12.7 mm, and gauge length of 9.5 mm were prepared by milling followed by sectioning on a high-speed saw. The specimens were polished up to 1200-grit SiC paper and finished with 0.3 μm alumina powder to eliminate surface defects. Tensile tests were conducted in air at room temperature using an MTS at an initial strain rate of $5\times10^{-4}\,s^{-1}$. Up to four tests were performed for each aging condition. Samples were preloaded to ~150 N prior to testing. Percent elongation was determined from measurements of the specimens taken before and after fracture using an optical microscope. True strain (ε) and true stress (σ) were calculated from the load–displacement data and the work-hardening exponent was determined using the Hollomon equation [21]: $\sigma=K(\varepsilon)^n$, where K is the strength coefficient that is equal to the true stress when $\varepsilon=1$, and n is the strain-hardening exponent. This equation can be rewritten $\log(\sigma)=\log(K)+n\log(\varepsilon)$. Thus, by plotting $\log(\sigma)$ versus $\log(\varepsilon)$ for the uniform plastic deformation range, and fitting a straight line to the data, n can be determined from the slope, i.e. $n=d\log(\sigma)/d\log(\varepsilon)$. For materials with inhomogeneous yielding, the plastic portion is considered starting from the lower yield point.

Image analysis was performed previously on particles in this alloy system that were aged up to 240 h [19]. The analysis was extended to samples that had been aged for 1325 h. The particle nearest-neighbor distance, λ was determined for each aging condition from the following equation [22]:

$$\lambda=\tfrac{1}{2}(P_A)^{-1/2}$$

where P_A is the particle density or point density and is equal to the particle count divided by the area of the image field of view [23]. Grain boundary coverage was calculated using BSE images. The percent coverage was found by subtracting segments of the grain boundary devoid of Laves and NiAl precipitates from the total grain boundary length and then dividing by the total grain boundary length.

X-ray diffraction (XRD) was also performed on bulk samples using a Rigaku D/Max 2000 diffractometer with Cu Kα radiation (λ=0.154059 nm) at 40 kV and 300 mA from 20° to 120° with a step size of 0.01° with a count time of 1 s per step.

3. Results and discussion

After solutionizing at 1250 °C the alloy is single phase austenite (f.c.c.) and after aging at 800 °C both Laves and NiAl phases are present [19]. Fig. 1 shows XRD patterns of the evolution of C14-type Fe_2Nb and B2-ordered NiAl precipitates in the austenitic matrix after a 1250 °C, 24 h solution heat treatment and subsequent aging at 800 °C for 2.4 h, 24 h, 240 h, and 1325 h. X-ray peaks corresponding to C14 and B2 phases were not clearly visible until 24 and 240 h, respectively.

Fig. 2 shows BSE images of the microstructures after the 1250 °C solution heat treatment and after aging at 800 °C for 0.5 h, 2.4 h, 24 h, 240 h, and 1325 h; the phase showing the light contrast is the C-14 type Fe_2Nb and the darker phase is the B2-structured NiAl. These precipitates are common in AFAs [1,5,6,9,24–29]. Fig. 2(b) shows that precipitation of the Laves phase occurs on the grain boundaries even within 30 min at 800 °C. Fig. 2(c) shows that after aging for 2.4 h at 800 °C NiAl precipitation accompanies the Laves phase precipitation on the grain boundaries, however, the Laves phase precipitates make up a majority of the grain boundary precipitates and are coarser than the Laves phase precipitates in the grain interior. After aging for 24 h (Fig. 2(d)) the Laves and NiAl precipitates have increased in size in the matrix and the NiAl grain boundaries and the amount of NiAl on the grain boundaries is now similar to the extent of Laves phase coverage. Fig. 2(e) shows that at 240 h the NiAl precipitates have significantly increased in size in the matrix compared to the Laves phase, but on the grain boundaries the Laves and NiAl particles are comparable in size. After aging for 1325 h (Fig. 2(e)) larger Laves phase particles are present in the matrix, and the size of the NiAl particles has also increased. As the aging time

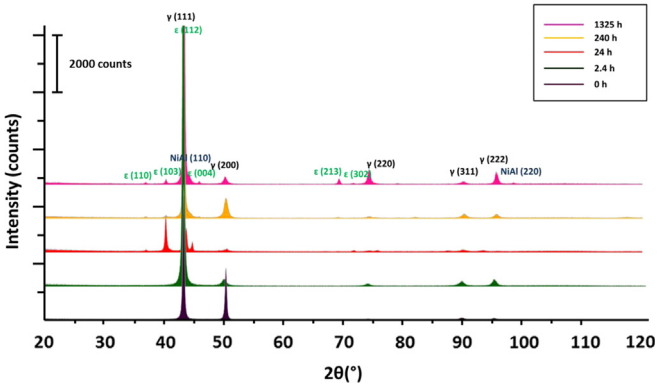

Fig. 1. XRD patterns of bulk samples of Fe–20Cr–30Ni–2Nb–5Al (at%) with visible peaks labeled ('γ', for the f.c.c. matrix, 'ε' for the Laves phase, 'NiAl' for the B2-NiAl phase) after a solution treatment and subsequent aging for 2.4, 24, 240, and 1325 h at 800 °C.

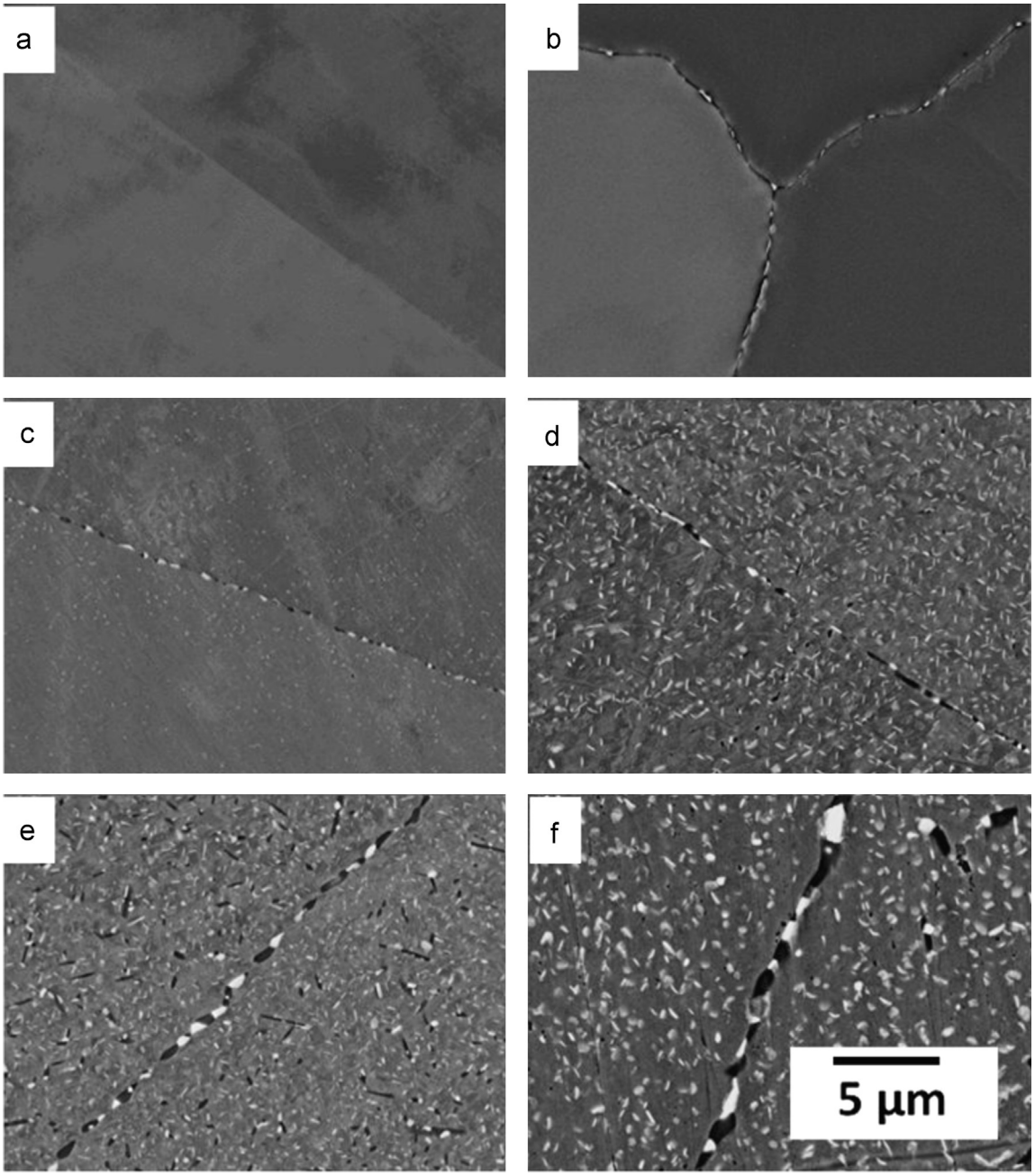

Fig. 2. BSE images showing matrix and grain boundary precipitation in Fe–20Cr–30Ni–2Nb–5Al (at%) after a solution treatment: (a) and aged at 800 °C for (b)0.5 h; (c) 2.4 h; (d) 24 h; (e) 240 h; and (f)1325 h. The light precipitates are the Laves phase and the dark precipitates are the B2 phase.

increased, a precipitation free zone (PFZ) becomes evident on the grain boundaries and increases in size. The formation of the precipitate free zone with longer aging is not surprising since the grain boundaries and matrix precipitates are made up of the same solute atoms [30]. In a 60 μm grain sized sample of Fe–20Cr–30Ni–2Nb–5Al (at%) that was examined after creep-rupture testing at 750 °C and 100 MPa, a γ′-PFZ was formed that was postulated to have caused low creep-ductility. It was suggested that coarsening the grain size or using directional solidification to reduce the total grain boundary area might improve creep properties [7].

Table 1 shows the average Laves and NiAl particle sizes both on the grain boundaries and within the matrix at each aging condition. The sizes of NiAl and Laves phase matrix precipitates for

Table 1
Average particle diameter for matrix and grain boundary Laves and NiAl precipitates for Fe–20Cr–30Ni–2Nb–5Al (at%) aged at 800 °C.

Aging time (h)	Average particle diameter (nm)			
	Laves		NiAl	
	Matrix	Grain boundary	Matrix	Grain boundary
2.4	95 ± 39*	192 ± 86	–	126 ± 75
24	205 ± 84*	332 ± 165	194 ± 103*	239 ± 124
240	252 ± 167*	355 ± 187	330 ± 149*	366 ± 187
1325	301 ± 170	743 ± 335	734 ± 668	864 ± 468

* Values from [19].

aging up to 240 h were reported in [19] and are duplicated in the Table. The Laves phase particles in the matrix after 24 h nearly doubled in size (205 nm) compared to the size at 2.4 h (95 nm). The Laves phase precipitates on the grain boundaries are 192 nm after aging for 2.4 h and show continued growth up to 743 nm after 1325 h. The NiAl particles are not visible in the matrix after 2.4 h, but appear on the grain boundaries (126 nm) and are slightly smaller than the Laves phase grain boundary precipitates (192 nm). Once NiAl precipitation is observed in the matrix at 24 h, the particle size continues to increase for aging times up to 1325 h: at 240 h the NiAl particle size (323 nm) is larger than that of the Laves phase (252 nm). At 240 h the grain boundary NiAl particles (366 nm) are also larger than the Laves phase particles on the grain boundaries (252 nm) and they continue to grow at a faster rate than the Laves phase grain boundary particles for aging up to 1325 h. After 1325 h the Laves phase particles showed growth to 301 nm in the matrix and the NiAl matrix particles had increased to 734 nm. In a Fe–20Cr–15Ni–5Al (at%) base alloy [16] the authors noted that after 2160 h at 800 °C there was not much change in the microstructure indicating good thermal stability. This thermal stability has also been noted after 2012 h at 750 °C in other AFA alloys [18].

Table 2 shows how the area fraction of grain boundary precipitates changes with time. While there is no grain boundary coverage without aging, after 2.4 h there is 56% grain boundary coverage. There is much more variability in grain boundary coverage after aging at 2.4 h. There is significant grain boundary coverage of 78% after 24 h and 84% after 240 h. After 1325 h the grain boundary was almost completely saturated with 93% coverage. At the early stages of aging, the amount of grain boundary precipitation significantly varies depending on the grain boundary misorientation. This is consistent with Denham and Silcock's observation that the size and density of the Fe_2Nb precipitates can show variations based on the crystallography of the grain boundary [31]. In the present alloy, as the grain boundary precipitates grew in size as the sample was aged, the boundaries that had less coverage initially were able to 'catch up' which led to increased grain boundary coverage as the sample was aged.

Table 2
Area fraction of grain boundary Laves and NiAl precipitates, room temperature yield strength (YS), ultimate tensile strength (UTS), and elongation to failure, ε_f, and strain-hardening exponent, n (with two n values in the case of two-stage work hardening), calculated over the uniform plastic range as a function of aging time at 800 °C for Fe–20Cr–30Ni–2Nb–5Al (at%).

Aging time (h)	Particle density (particles/μm²)	GB area fraction (%)	YS (MPa)	UTS (MPa)	ε_f (%)	Strain-hardening exponent (n)	
0	0	0	205	338	52	0.13	0.61
2.4	0.476	56	322	502	37	0.61	
24	1.809	78	362	707	29	0.31	
240	1.173	84	351	715	28	0.27	
1325	1.340	93	383	736	19	0.29	

Fig. 3(a) is a bright field TEM image showing dislocations surrounding the Laves phase precipitates. Dislocations can be punched out due to the strains arising from the difference in the thermal expansion between the precipitate and matrix. The dislocations formed from the precipitation of the Laves phase then act as sites for further Laves phase precipitation and can result in the formation of stringers [30]. Evidence of precipitation in this manner is visible in the BSE image shown in Fig. 3(b) where in one grain, there are lines of precipitates that have presumably precipitated on punched out dislocations. The strain contrast that is present in TEM images of Fe_2Nb that has precipitated in austenite in Fe–20Cr–35Ni–2Nb and Fe–20Cr–25Ni–2Nb (at%) after aging at 800 °C [17] is indicative of a semi-coherent precipitate-matrix interface and may be a reason why the Laves phase has shown stability during aging and creep testing at 800 °C [32]. If the precipitate had a different crystal structure than the matrix it would be expected to form a needle-like or disk-like nucleus [33].

Tensile testing showed that the strength and ductility of the alloy was strongly influenced by the aging time and, hence, the formation and coarsening of the precipitates. Increasing the aging time led to an increase in tensile strength, but a decrease in ductility, see Fig. 4. Fig. 5 shows BSE images of the fracture surfaces after tensile testing, which all displayed dimple-type ductile rupture irrespective of the measured elongations. The trends of decreased ductility and improved strength with ageing observed here have been noted in other AFA alloys aged at 750 °C [18]. In AFA alloys with base composition Fe–(11.90–14.24)Cr–1.93Mn–(20.10–25.24)Ni–(0.47–0.48)Cu–(2.87–3.91)Al–14Si–(1.01–1.00)Nb–(2–2.01)Mo–(1–0.99)W (wt%) yield strength and ultimate tensile strength reached maximum values (400–450 and 890–930 MPa respectively) after 50 or 500 h aging and the yield strength did not show much change, while the ultimate tensile strength slightly decreased. Among the AFA alloys tested, elongation continuously decreased with aging regardless of composition [18]. In contrast to

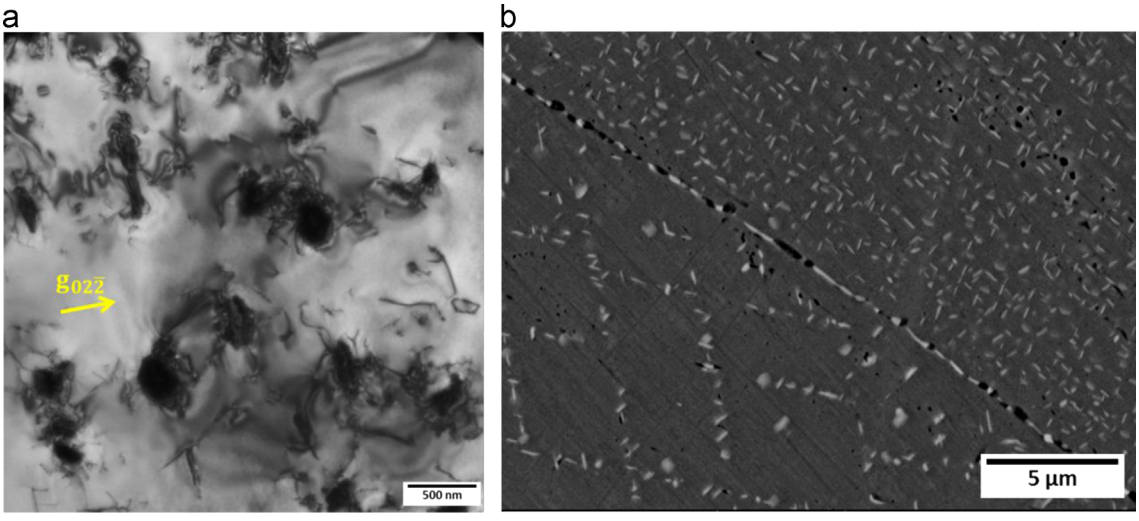

Fig. 3. (a) Bright field TEM image showing dislocations punched out at Laves phase precipitates in Fe–20Cr–30Ni–2Nb–5Al (at%) aged for 2.4 h at 800 °C; and (b) BSE image showing lines of Laves Phase precipitates in sample aged for 24 h at 800 °C that have likely formed on dislocations.

other heat treatment conditions, the tensile test curves after aging for 2.4 h were discontinuous and showed an upper and lower yield point with a Lüder's strain of 5%. This yield-point phenomenon has been studied extensively in steels and is known to occur when dislocations quickly multiply and the average dislocation velocity decreases along with the stress needed to move dislocations [34–36]. A summary of the yield strength, ultimate tensile strength and elongation for each aging condition is presented in Section 2. When an upper and lower yield strength was observed, the lower yield strength is presented.

Figs. 6 and 7 show representative plots of the strain hardening exponent fit for the different aging conditions. The n value can range from 0 to 1 with typical values being from 0.1 to 0.6 [37]. In Fig. 6 the double logarithmic plot of the true stress and true strain for the solutionized alloy did not show a good straight line fit, while linear fits with R^2 values close to 1 were obtained for aging times of 2.4 h, 24 h, 240 h and 1325 h (Fig. 7), i.e. except for the as-solutionized alloy, all the other specimens could be well described by the Hollomon equation. Hollomon noted that there were cases where the log–log plots of stress and strain can curve upward, especially for larger strains, suggesting anisotropy [21]. The homogenized, non-aged alloy showed the largest elongation. Fig. 6 shows that this alloy displayed two-stage work hardening also known as 'double n' behavior. The curve is deconvoluted to show two stages of work-hardening with the first curve showing a small n-value of 0.18 followed by a second stage showing a high n value of 0.70. The representative log–log plots in Fig. 7 for samples aged at 2.4 h, 24 h, 240 h and 1325 h show a good match to the Holloman equation all with R^2 values of 0.99. Samples aged at 2.4 h showed the highest work-hardening exponent with $n=0.62$. This is most likely due to the effects of discontinuous yielding. The n value for steels typically decreases with increasing strength. The highest possible n value of a steel is when its strength is the lowest and n tends to increase with elongation [38]. In the present study, n-values after aging at 24 h, 240 h and 1325 h were ~0.3. The strain hardening values are summarized in Table 2.

Fig. 8 shows a linear fit to a plot of the inverse mean surface-to-surface interparticle spacing versus the yield strength, which produces the equation σ_y (MPa)$=74\lambda^{-1}+202$ where λ is the mean interparticle spacing. The predicted value of the yield strength from this equation without any particles at 202 MPa is closely similar to the experimentally-measured value of 205 MPa. The result is indicative of a looping mechanism of particle strengthening. An Orowan looping-based mechanism would make sense for the Laves phase precipitates because they are hard and brittle and would act as a barrier to dislocation motion [18]. The model does not, however, completely capture the results obtained. The largest YS and UTS were observed after 1325 h, not after 24 h when the smallest interparticle spacing was observed.

It is possible that the greater grain boundary coverage at 1325 h is what caused the alloy to show both higher yield and tensile strength even as the matrix particles coarsened and the inter-particle distance increased. Tarigan et al. reported that creep life was extended without ductility loss even with increased Laves phase grain boundary precipitation in Fe–20Cr–30Ni–2Nb (at%) [14,15] and called the strengthening mechanism a "grain boundary precipitation strengthening mechanism" (GBPS) which they

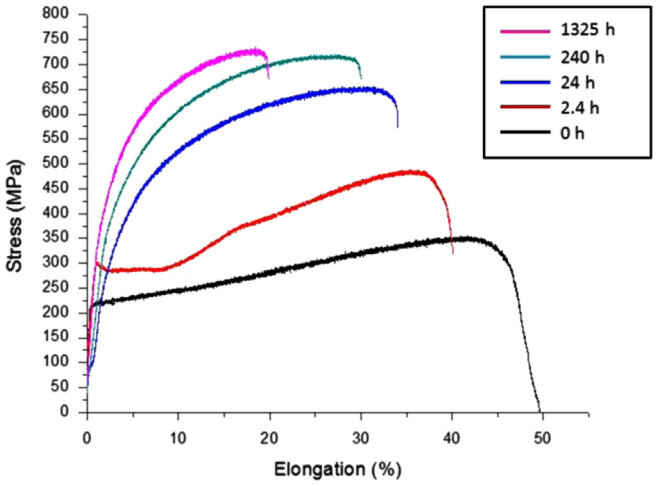

Fig. 4. Representative tensile curves of Fe–20Cr–30Ni–2Nb–5Al (at%) solutionized at 1250 °C for 24 h and subsequently aged at 800 °C for different times as indicated. At least three tests were performed for each condition.

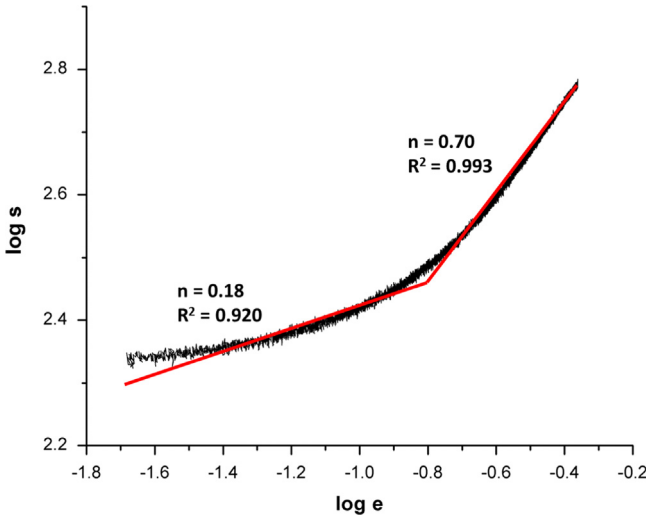

Fig. 6. Two-stage work hardening in log–log plot of true stress versus true strain for the entire uniform plastic range for as-solutionized Fe–20Cr–30Ni–2Nb–5Al (at%).

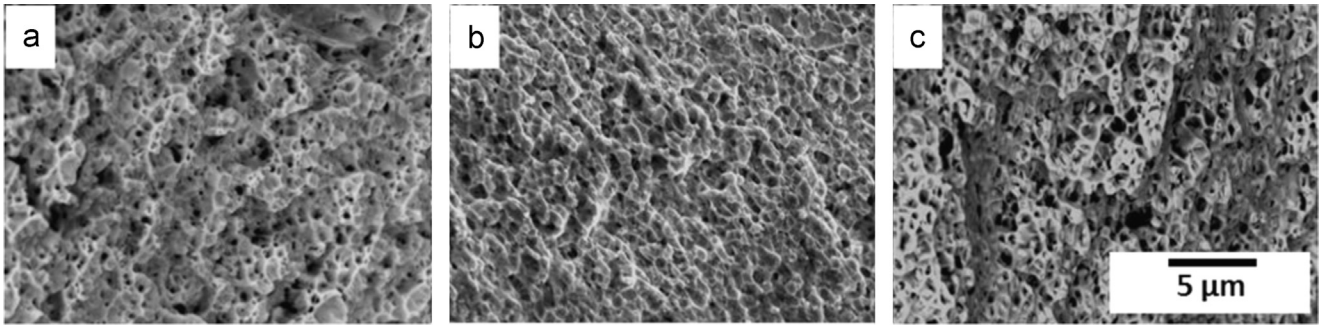

Fig. 5. Fracture surfaces of Fe–20Cr–30Ni–2Nb–5Al (at%) after aging at 800 °C for (a) 2.4 h; (b) 240 h; and (c) 1325 h.

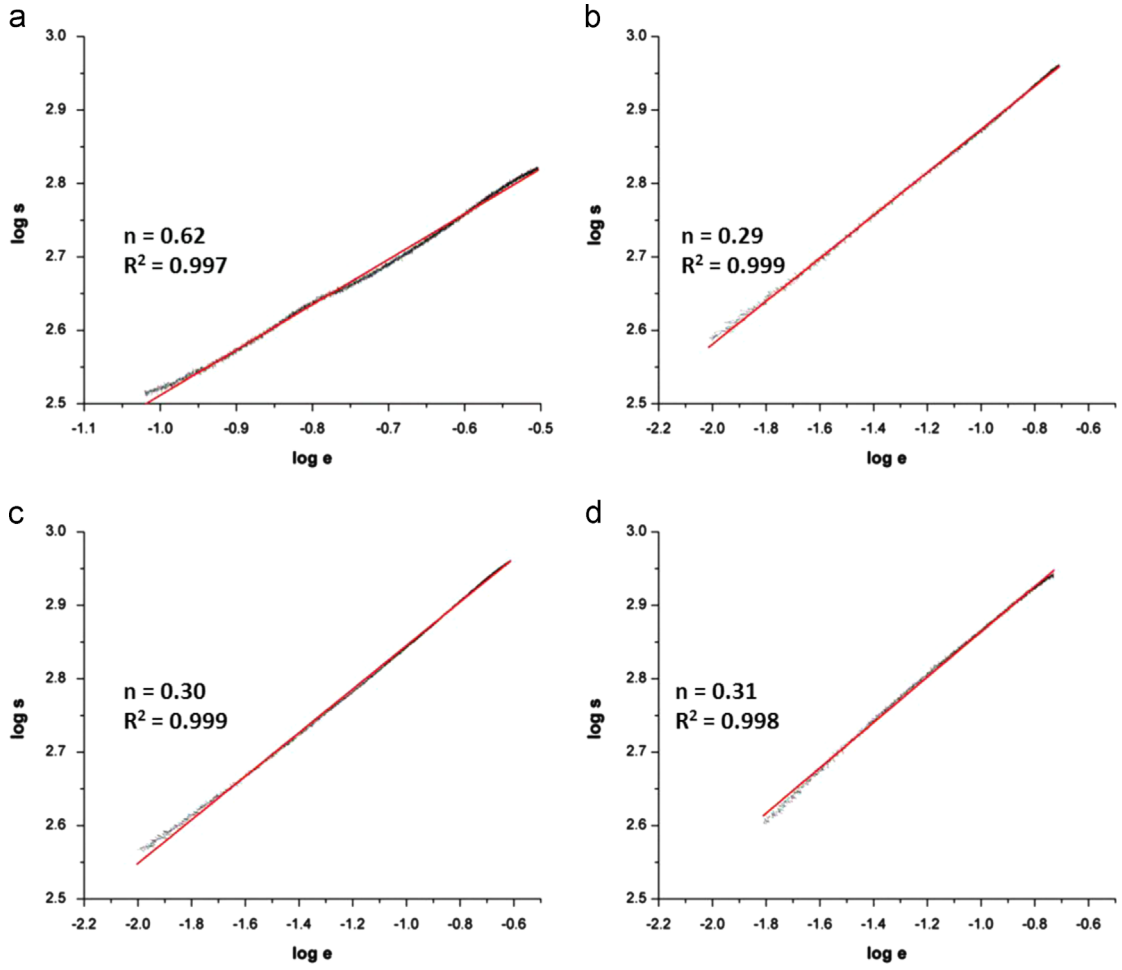

Fig. 7. Representative log–log plots of true stress versus true strain in the uniform plastic range for Fe–20Cr–30Ni–2Nb–5Al (at%) aged at 800 °C with corresponding stress components and R^2 values for (a) 2.4 h; (b) 24; (c) 240 h and (d) 1325 h.

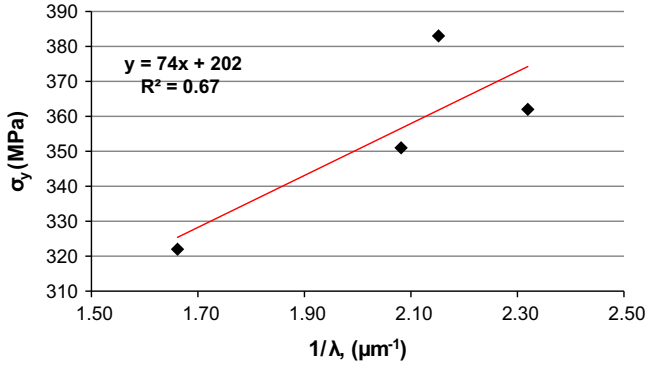

Fig. 8. Yield strength vs. inverse interparticle spacing for Fe–20Cr–30Ni–2Nb–5Al (at%).

proposed was caused by decreased grain boundary deformation in sections of the grain boundary covered by the Laves phase. In Chen et al.'s study of Fe–20Cr–30Ni–2Nb–0.03B (at%) it was also concluded that precipitation of the Laves phase on the grain boundaries enhanced creep resistance [10]. These alloys did not include additions of Al so instead of just Laves phase, both Laves and NiAl precipitates are present on the matrix and grain boundary. Consistent with the results involving creep, the yield strength and ultimate tensile strength maximum at 1325 h in Fe–20Cr–30Ni–2Nb–5Al (at%) reflects the condition of maximum grain boundary coverage, indicating that the increased grain boundary precipitation acted as a more effective barrier to dislocations. After 24 h, when over 78% of the grain boundaries were covered with precipitates, in spite of a decreased interparticle distance, the yield strength and ultimate tensile strength showed a relatively small increase up to the 1325 h aging time, compared to the initial increase in strength from the precipitation observed at 2.4 h. The 93% grain boundary coverage at 1325 h, coupled with the more than doubling and tripling of grain boundary precipitate size at 24 h for the Laves and NiAl, respectively led ductility to decrease by ~1/3.

Even with the grain boundaries being nearly completely saturated with precipitates of brittle phases, the alloy had ductility of 19% after 1325 h. If the two phases are relatively coherent with the grain boundary, it would be expected that a favorable combination of creep and ductility could be attained [39]. For example, data from Keown and Pickering's on AISI type 347 stainless steels in 1974 [40] suggested that the Fe_2Nb on grain boundaries might have improved creep ductility, but Kestenbach and Bueno [39] presented evidence that disproved this. They also cited that Fe_2Nb precipitation caused decreased ductility in the high temperature tensile tests performed by Denhan and Silcock [31]. However, in Bei et al.'s more recent study of AFAs, even though the ductility decreased with aging, it was still 10–15% in room temperature tensile tests after aging for 2012 h, even though there was extensive grain boundary coverage of both NiAl and Laves phases [18]. Tarigan et al. [14,15] observed that even with 89% grain boundary coverage by the Laves phase precipitates a creep rupture strain of 77% was attained which suggests that Laves phase grain boundary precipitates do not necessarily lead to deleterious embrittlement. The most often cited Laves phase

orientation relationship with austenite achieves a 5% contraction of the matrix in the [111] direction and 9% expansion in the [112] direction [31] which represents a moderate misfit when compared to high misfit particles such as niobium carbonitride (~23% mismatch with the austenite matrix [41]) which can reduce creep ductility. In an Fe–Ni–Cr–Al (FNCA) alloy with a similar base composition to the alloy in the present study that did not include niobium, two variants of the Kurdjmov–Sachs relationship were found for NiAl [42]. If present in this alloy, this relationship might achieve a misfit with the matrix that would encourage ductility despite extensive grain boundary precipitation. If the more oft observed orientation relationships for NiAl and Laves phases are consistent for Fe–20Cr–30Ni–2Nb–5Al (at%), this may explain why the coverage of the grain boundaries with these brittle precipitates might lead to sufficient ductility.

4. Summary

The microstructural and mechanical response to aging Fe–20Cr–30Ni–2Nb–5Al (at%) at 800 °C after a 1250 °C solution heat treatment was studied. With aging the Laves phase particles at first grew rapidly in the matrix and after 24 h showed steady growth to 301 nm after 1325 h. The NiAl matrix particles after 24 h were only 90 nm at the 24 h time interval and grew relatively quickly up to 734 nm after 1325 h. Both Laves and NiAl particles grew substantially on the grain boundaries and more than doubled in size as the sample was aged from 240 to 1325 h.

Tensile tests were performed and the strain-hardening exponent generally showed a good fit to the Holloman equation. The unaged alloy showed two-stage work hardening. When the alloy was aged at 2.4 h an upper and lower yield point was observed. Improved strength was observed with increased grain boundary precipitation as the sample was aged, reaching a maximum of 383 MPa at 1325 h even though the interparticle spacing decreased.

Even as the grain boundary precipitate coverage increased to 93% after 1325 h the alloy showed room temperature elongation of 19%. It was hypothesized that the ductility in the alloy may be related to the low-misfits of the precipitates with the austenite matrix.

Acknowledgments

This research was supported by National Science Foundation Grant DMR 1206240. Any opinions, findings, and conclusions or recommendations expressed in this material are those of the author(s) and do not necessarily reflect the views of the National Science Foundation.

References

[1] M.P. Brady, J. Magee, Y. Yamamoto, D. Helmick, L. Wang, Mater. Sci. Eng.: A 590 (2014) 101–115.
[2] P. Kofstad, Oxid. Met. 44 (1995) 3–27.
[3] U. Heubner, Nickel Alloys, CRC Press, Boca Raton, 2000.
[4] J.A. McGurty, Google Patents, 1978.
[5] Y. Yamamoto, M.P. Brady, Z.P. Lu, P.J. Maziasz, C.T. Liu, B.A. Pint, K.L. More, H.M. Meyer, E.A. Payzant, Science 316 (2007) 433–436.
[6] M. Brady, Y. Yamamoto, M. Santella, P. Maziasz, B. Pint, C. Liu, Z. Lu, H. Bei, J. Miner. Met. Mater. Soc. 60 (2008) 12–18.
[7] Y. Yamamoto, M. Takeyama, Z.P. Lu, C.T. Liu, N.D. Evans, P.J. Maziasz, M.P. Brady, Intermetallics 16 (2008) 453–462.
[8] Y. Yamamoto, M.P. Brady, M.L. Santella, H. Bei, P.J. Maziasz, B.A. Pint, Metall. Mater. Trans. A 42 (2011) 922–931.
[9] Y. Yamamoto, G. Muralidharan, M.P. Brady, Scr. Mater. 69 (2013) 816–819.
[10] S.W. Chen, C. Zhang, Z.X. Xia, H. Ishikawa, Z.G. Yang, Mater. Sci. Eng.: A 616 (2014) 183–188.
[11] C.S. Barrett, T. Massalski, Structure of Metals, 3rd revised edition: Crystallographic Methods, Principles and Data, Pergamon Press, Oxford 1980.
[12] Y. Kato, M. Ito, Y. Kato, O. Furukimi, Mater. Trans. 51 (2010) 1531–1535.
[13] N.G. Masao Takeyama, Sumio Morita, Takashi Matsuo, MRS Proc. 842 (2004).
[14] I. Tarigan, N. Takata, Y. Terada, M. Takeyama, Proceedings of the 12th International Conference on Creep and Fracture of Engineering Materials and Structures (JIMIS 11), The Japan Institute of Metals, Kyoto, Japan, May 27–31, 2012.
[15] K.K. Imanuel Tarigan, Naoki Takata, Takashi Matsuo, Masao Takeyama, MRS Proc. 1295 (2011) 317–322.
[16] Y. Yamamoto, M.P. Brady, Z.P. Lu, C.T. Liu, M. Takeyama, P.J. Maziasz, B.A. Pint, Metall. Mater. Trans. A 38 (2007) 2737–2746.
[17] M. Takeyama, Mater. Sci. Forum 539–543 (2007) 3012–3017.
[18] H. Bei, Y. Yamamoto, M.P. Brady, M.L. Santella, Mater. Sci. Eng.: A 527 (2009) 2079–2086.
[19] G. Trotter, G. Rayner, I. Baker, P.R. Munroe, Intermetallics 53 (2014) 120–128.
[20] W. Rasband, Astrophysics Source Code Library, 1, 2012, 06013.
[21] J.H. Hollomon, AIME Trans. 12 (1945) 1–22.
[22] K.J. Kurzydlowski, B. Ralph, The Quantitative Description of the Microstructure of Materials, CRC Press, Boca Raton, 1995.
[23] E.F. Prados, V.L. Sordi, M. Ferrante, Acta Mater. 61 (2013) 115–125.
[24] M.P. Brady, Y. Yamamoto, M.L. Santella, B.A. Pint, Scr. Mater. 57 (2007) 1117–1120.
[25] B.A. Pint, M.P. Brady, Y. Yamamoto, M.L. Santella, J.Y. Howe, R. Trejo, P.J. Maziasz, Proceedings of ASME Turbo Expo 2009: Power for Land, Sea and Air (GT2009), vol. 5, 2009, pp. 271–280.
[26] B.A. Pint, J.P. Shingledecker, M.P. Brady, P.J. Maziasz, Proceedings of ASME Turbo Expo 2009: Power for Land, Sea and Air (GT2007), vol. 3, 2007, pp. 995–1002.
[27] M.P. Brady, Y. Yamamoto, M.L. Santella, L.R. Walker, Oxid. Met. 72 (2009) 311–333.
[28] Y. Yamamoto, M.L. Santella, M.P. Brady, H. Bei, P.J. Maziasz, Metall. Mater. Trans. A 40 (2009) 1868–1880.
[29] D.Q. Zhou, X.Q. Xu, H.H. Mao, Y.F. Yan, T.G. Nieh, Z.P. Lu, Mater. Sci. Eng.: A 594 (2014) 246–252.
[30] J.W. Martin, Precipitation Hardening, Butterworth-Heinemann, Oxford, United Kingdom, 1998.
[31] A. Denham, J. Silcock, J. Iron Steel Inst. 207 (1969) 582–592.
[32] M.P. Brady, Y. Yamamoto, Z.P. Lu, C.T. Liu, P.J. Maziasz, B.A. Pint, US Patent Disclosure, 2007.
[33] D.A. Porter, K.E. Easterling, Phase Transformations in Metals and Alloys, CRC Press, Boca Raton, 2009.
[34] B. Vargas-Arista, C. Angeles-Chavez, A. Albiter, J.M. Hallen, Mater. Charact. 60 (2009) 1561–1568.
[35] R. Abbaschian, R. Reed-Hill, Physical Metallurgy Principles – SI Version, Cengage Learning, Stamford, 2009.
[36] J.R. Davis, Tensile Testing, 2nd ed., ASM International, Materials Park, Ohio, 2004.
[37] W.F. Hosford, Mechanical Behavior of Materials, Cambridge University Press, New York, 2005.
[38] D. Llewellyn, R. Hudd, Steels: Metallurgy and Applications: Metallurgy and Applications, Butterworth-Heinemann, London, 1998.
[39] H.J. Kestenbach, L.O. Bueno, Mater. Sci. Eng. 66 (1984) L19–L23.
[40] S. Keown, F. Pickering, Creep Strength in Steel and High-Temperature Alloys, The Metals Society, London, 1974.
[41] B. Dutta, C. Sellars, Mater. Sci. Technol. 3 (1987) 197–206.
[42] D.V.V. Satyanarayana, G. Malakondaiah, D.S. Sarma, Mater. Charact. 47 (2001) 61–65.